Supplementary Information

A Two-electron Transfer Mechanism of Zn-doped δ-MnO_2 Cathode toward Aqueous Zn-ion Batteries with Superhigh Capacity

*Wen Zhao[1], Jared Fee[2], Harshul Khanna[1], Seth March[2], Nathaniel Nisly[2], Samantha Joy B. Rubio[2], Can Cui[1], Zhuo Li[3] and Steven L. Suib[1, 2, *]*

1. Department of Materials Science and Engineering & Institute of Materials Science, University of Connecticut, 97 N. Eagleville Rd., Storrs, Connecticut 06269-3136, United States

2. Department of Chemistry, University of Connecticut, 55 N. Eagleville Rd., Storrs, Connecticut 06269-3060, United States

3. Department of Materials Science and Engineering, Huazhong University of Science and Technology, Wuhan 430074, P. R. China.

* Email: steven.suib@uconn.edu

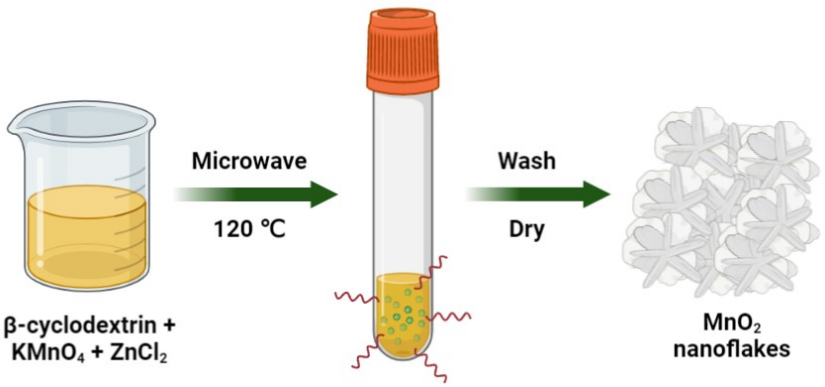

Figure S1. The simplified schematic fabrication process of Zn-doped δ-MnO_2.

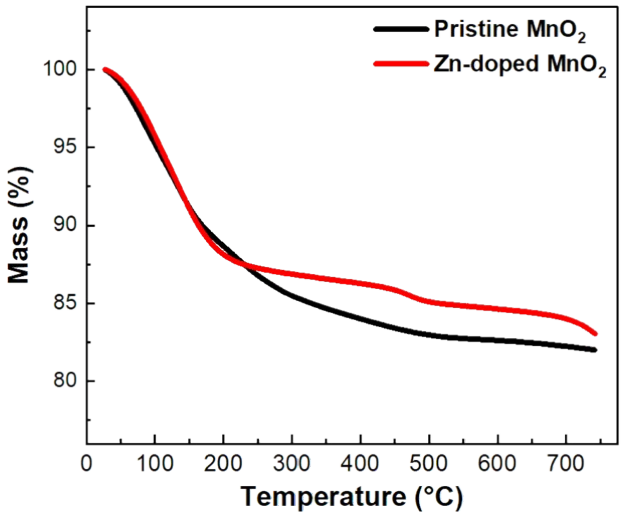

Figure S2. TGA profiles of pristine and Zn-doped MnO_2 samples from 27 to 750 °C.

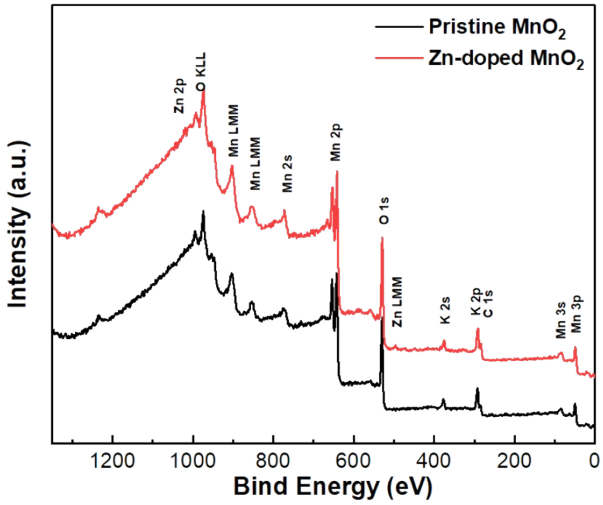

Figure S3. Full-scan XPS spectra of pristine and Zn-doped MnO_2.

Table S1. XRF analysis results of pristine and Zn-doped MnO_2 samples.

Samples	Mol % K	Mol % Mn	Mol % Zn	Formula
Pristine MnO_2	18.9%	81.1%	0	$K_{0.19}MnO_2$
Zn-doped MnO_2	18.3%	80.3%	1.4%	$K_{0.18}Zn_{0.014}MnO_2$

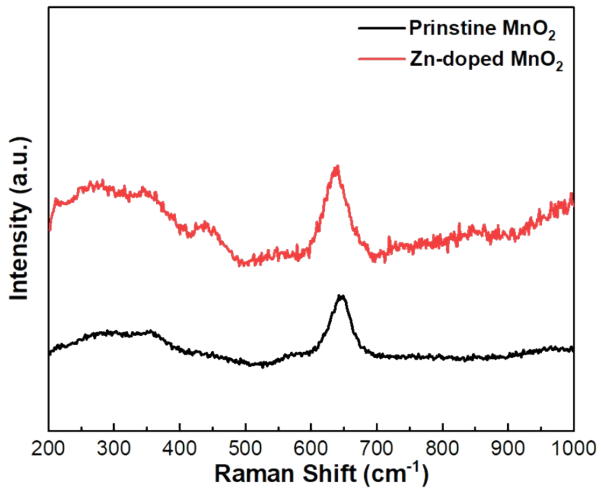

Figure S4. Raman spectra of pristine and Zn-doped MnO_2 materials.

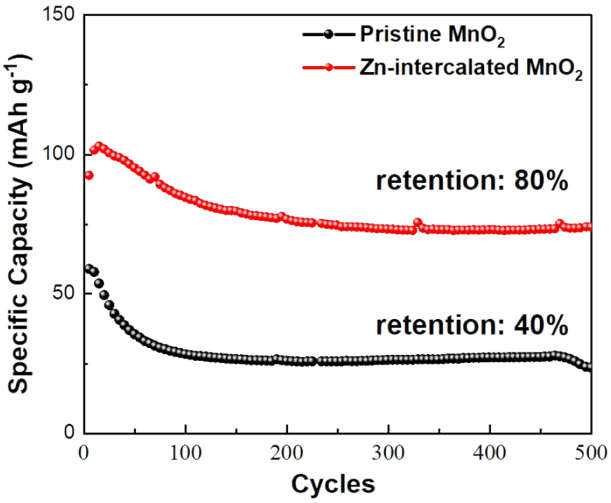

Figure S5. Cycling performance of pristine and Zn-doped MnO_2 ZIBs at 200 mA g^{-1} for 500 cycles.

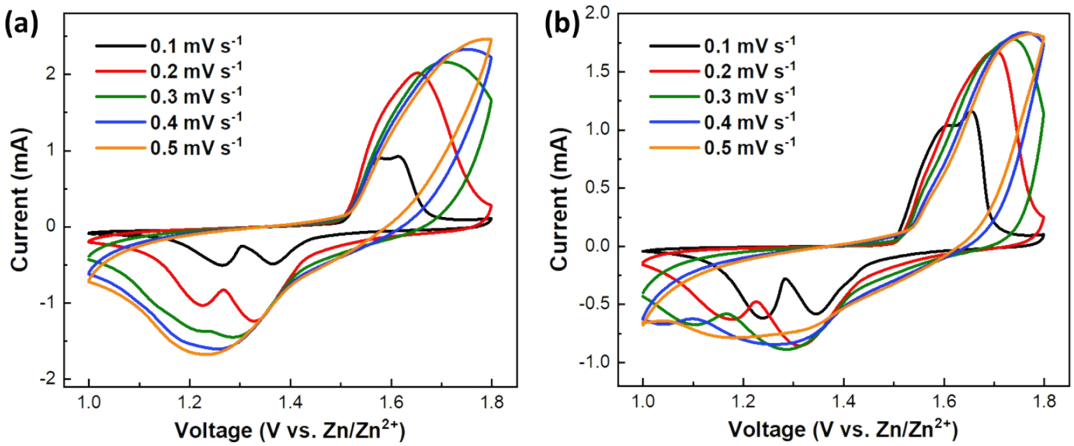

Figure S6. CV curves of (a) Zn-doped MnO_2 and (b) pristine MnO_2 ZIBs at various scan rates.

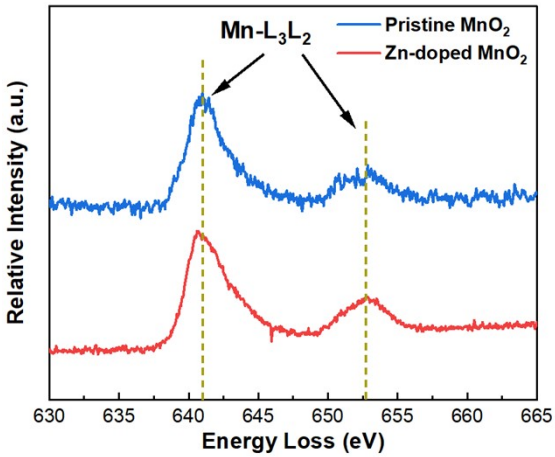

Figure S7. The EELS profiles of manganese $L_{2,3}$ edges of pristine and Zn-doped MnO_2 cathodes discharged to 1V.

Fig. S7 shows electron energy-loss spectroscopy (EELS) spectra of pristine and Zn-doped MnO_2 cathodes discharged to V5 (1.0 V). In general, the excitation edges shift to lower energy-loss for a lower oxidation state and the integral intensity ratio of L_3 and L_2 excitation peaks of Mn is correlated to its oxidation state. Compared to the standard Mn^{4+} spectrum, the L_3 peak maximum exhibits lower energy losses (Zn-doped MnO_2: 640.95 eV; pristine MnO_2: 641.05 eV), and the $I(L_3)/I(L_2)$ white line intensity ratios (Zn-doped MnO_2: 3.50; pristine MnO_2: 3.46) correspond to a mixed valency of Mn^{2+} and Mn^{3+}, confirming the existence of Mn^{2+} in electrodes.[1,2]

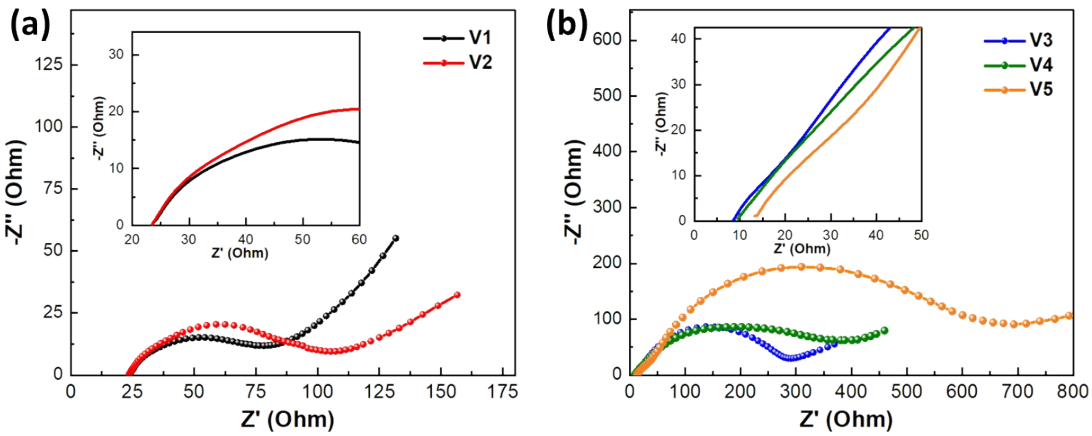

Figure S8. Nyquist plots of Zn-doped MnO_2 ZIBs at different voltages vs. Zn^{2+}/Zn: (a) V1 (1.8 V) and V2 (1.44 V); (b) V3 (1.31 V), V4 (1.28 V) and V5 (1.0 V)

Compared with the charge transfer resistance (R_{ct}) at OCV (~1.5 V vs Zn^{2+}/Zn), the R_{ct} at 1.31 V became larger in Zn-doped MnO_2 ZIBs, while the R_{ct} of pristine MnO_2 ZIBs decreased slightly. To evaluate the ohmic resistance changes with voltage changes, we performed EIS on Zn-doped MnO_2 ZIBs at different voltages. Fig. S6a shows the Nyquist plots of Zn-doped MnO_2 ZIBs at V1-V5. The ohmic resistance of ZIBs increased with both H^+ and Zn^{2+} insertion. The smaller R_{ct} at 1.31 V than that at OCV in pristine MnO_2 ZIBs may be due to the intercalation of Zn ions into the δ-MnO_2 crystal structure, which is similar to the role of zinc doping.

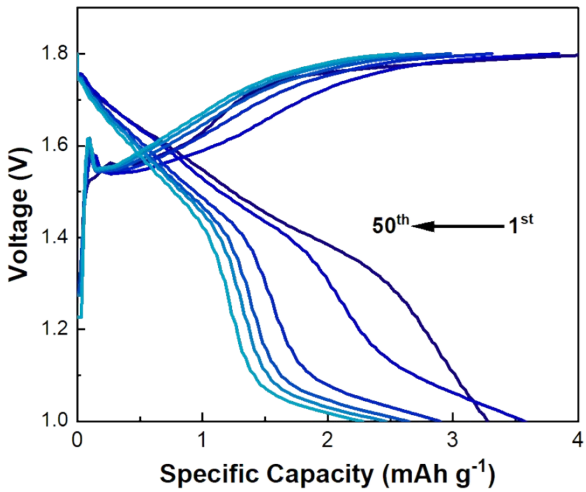

Figure S9. Charge/discharge curves of cathode-free ZIBs for 50 cycles at a low current of 0.06 mA.

Calculation of the theoretical capacity

The theoretical capacity is calculated using the equation:

$$C_t = \frac{nF}{3600 \times M} \quad (1)$$

Where n is the number of electrons involved in the electrochemical reactions, F is Faraday Constant (96485.34 C mol^{-1}), and M is molecular weight (g mol^{-1}).

Calculation of the specific energy

Due to the excess Zn foil anode, ZIBs use the mass of active cathode materials to calculate the energy density. The equation is provided below:

$$E = \frac{\int_0^{t_{cutoff}} (V(t) \times i)dt}{3600} \quad (2)$$

where *V(t)* is voltage (function of time, V), *i* is the current density (mA g^{-1}), and t_{cutoff} is the cutoff time. Graphically, it is the area under the voltage vs. specific capacity curve.

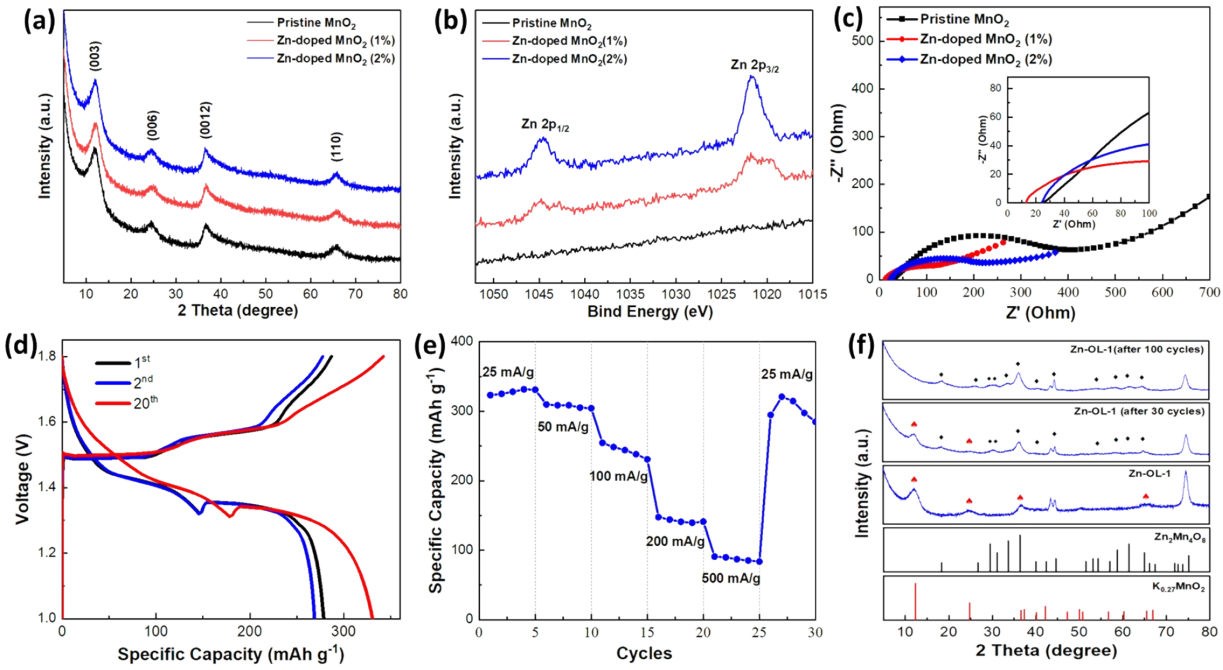

Figure S10. (a) XRD patterns, (b) high-resolution Zn 2p XPS spectra, (c) Nyquist plots of pristine, 1 % and 2% Zn-doped δ-MnO_2. (d) Discharge-charge profiles and (e) rate performance of 2% Zn-doped MnO_2 ZIBs. (f) XRD patterns of 2% Zn-doped MnO_2 cathodes at the 30th and 100th discharged states.

We prepared pure δ-MnO_2, 1% and 2% Zn doped δ-MnO_2. Fig. S10a shows the XRD patterns of all three materials and 2% Zn doped MnO_2 has the similar crystallographic structure as both pristine and 1% Zn doped MnO_2. The high-resolution Zn 2p spectra in Fig. S10b confirm the increasing amount of Zn doping in 2% doped MnO_2 samples. Additionally, the amount of Zn doping in 2% doped samples was evaluated to be 2.7 mol % by XRF characterization, which is higher than that in 1% Zn doped samples (1.4 mol %). EIS data in Fig. S10c indicates that 1% doped MnO_2 cathode has the smallest electron transfer resistance (R_{ct}) and the highest ion diffusion rate, which should provide the best reaction kinetics. For 2% doped MnO_2 ZIBs, a maximum discharge capacity of 331 mAh g^{-1} was achieved after 20 cycles at 25 mA g^{-1}, as shown in Fig. S10d. The highest specific capacity and the rate performance (Fig. S10e) of 2% doped MnO_2 ZIBs are better than that of pristine MnO_2 ZIBs, but inferior to that of 1% Zn-doped MnO_2 ZIBs. Moreover, the XRD patterns of 2% doped MnO_2 cathodes at discharged states after different cycles in Fig. S10f show that the birnessite MnO_2 phase is still retained after 30 cycles of charge/discharge procedures, but is completely transferred to $Zn_2Mn_4O_8$ after 100 cycles. Based on the characterization of materials and electrochemical measurement results, the content of Zn in the Zn-doped MnO_2 sample was optimized to be 1%.

Table S2. Comparison of electrochemical performances of the Zn-doped MnO_2 cathodes with reported cathode materials in aqueous zinc-ion batteries.

Cathode	Electrolyte	Potential (V)	Specific Capacity (mAh g^{-1})	Specific Energy (W h Kg-1)	Ref.
Zn-doped MnO_2	2 M $ZnSO_4$+0.2 M $MnSO_4$	1.0-1.8	455	628	This work
α-(Mn_2O_3–MnO_2)	2 M $ZnSO_4$+0.15 M $MnSO_4$	0.9-1.9	183	187.5	3
$Cu_3(HHTP)_2$	3M $Zn(CF_3SO_3)_2$	0.5-1.5	228	–	4
$(NH_4)_2V_{10}O_{25}$	3M $Zn(CF_3SO_3)_2$	0.4-1.5	408	287	5
MnO/C@rGO	2 M $ZnSO_4$+0.1 M $MnSO_4$	0.8-1.9	315	–	6
δ-MnO_2	$ZnSO_4$-based gel electrolyte	0-2.0	324	531	7
$K_{0.8}Mn_8O_{16}$	2 M $ZnSO_4$+0.1 M $MnSO_4$	1.0-1.9	317	436	8
α-$K_{1.33}Mn_8O_{16}$	2 M $ZnSO_4$+0.1 M $MnSO_4$	0.8-1.9	320	398	9
δ-MnO_2/Graphite	1 M $ZnSO_4$	1.0-1.8	235	–	10
Defect-enriched MnO_2	2 M $ZnSO_4$+0.1 M $MnSO_4$	1.0-1.9	388	406	11
γ-MnO_2	1 $Zn(CH_3COO)_2$+0.4 $Mn(CH_3COO)_2$	1.0-1.8	556	–	12
ε-MnO_2	2 M $ZnSO_4$+1 M $MnSO_4$+0.1 M H_2SO_4	1.0-1.95	570	409	13
ε-MnO_2	2.5 M H_2SO_4+0.5 M $MnSO_4$	1.0-2.8	616	1621.7	14

The (–) symbol signifies that the information has not been reported.

Table S3. The fitted results of electrolyte resistance (R_s) and charge-transfer resistance (R_{ct}) of pristine and Zn-doped MnO_2 ZIBs. OCV: open circuit voltage

Samples		R_s	R_{ct}
Pristine MnO_2	OCV	25.4	407.4
	1.31 V vs. Zn^{2+}/Zn	12.3	348.4
Zn-doped MnO_2	OCV	11.6	132.3
	1.31 V vs. Zn^{2+}/Zn	8.9	294.2

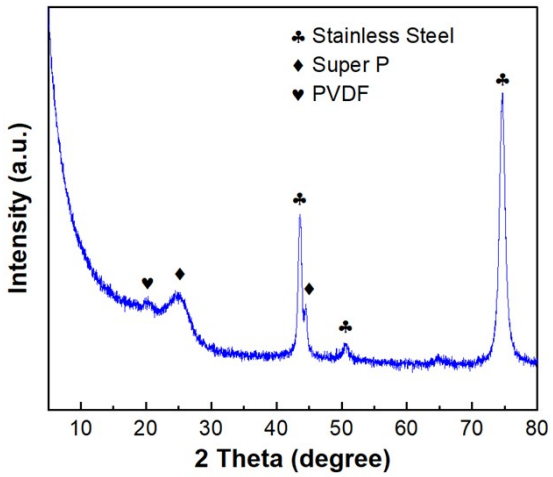

Figure S11. XRD patterns of the reference electrode with Super P and PVDF coated on the stainless-steel substrate.

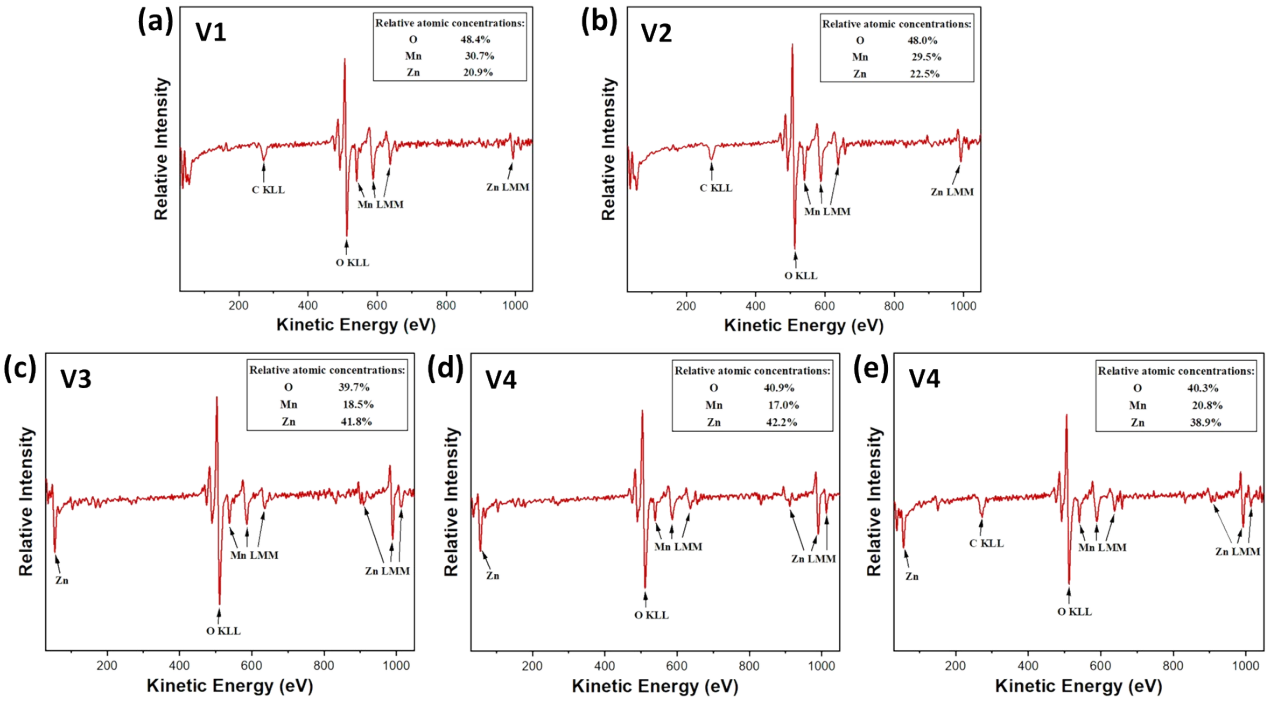

Figure S12. Relative atomic concentration of Zn-doped MnO_2 cathodes at different states via AES.

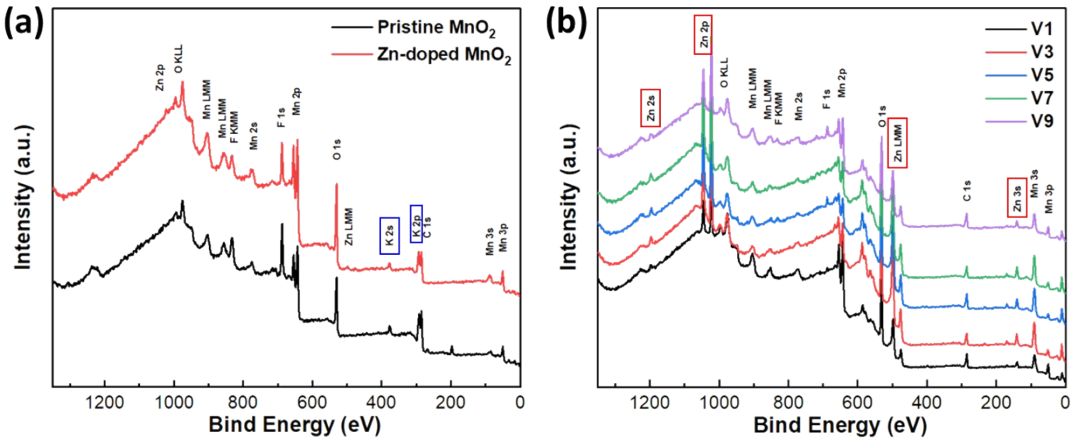

Figure 13. (a) Full-scan XPS spectra of pristine and Zn-doped MnO_2 cathodes. (b) Full-scan XPS spectra of Zn-doped MnO_2 cathodes at different states.

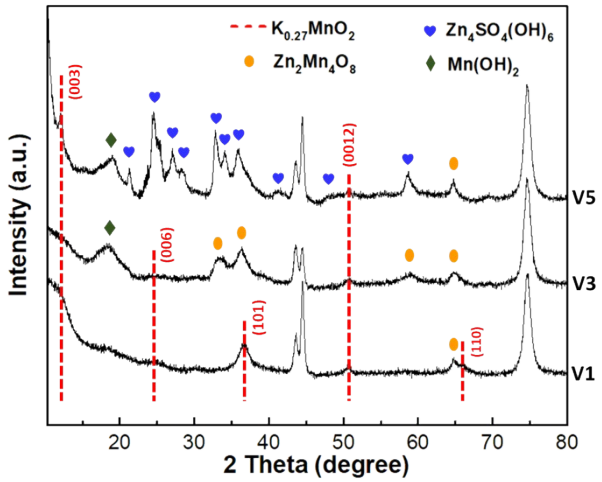

Figure S14. *Ex situ* XRD patterns of pristine MnO_2 cathodes during the discharge process.

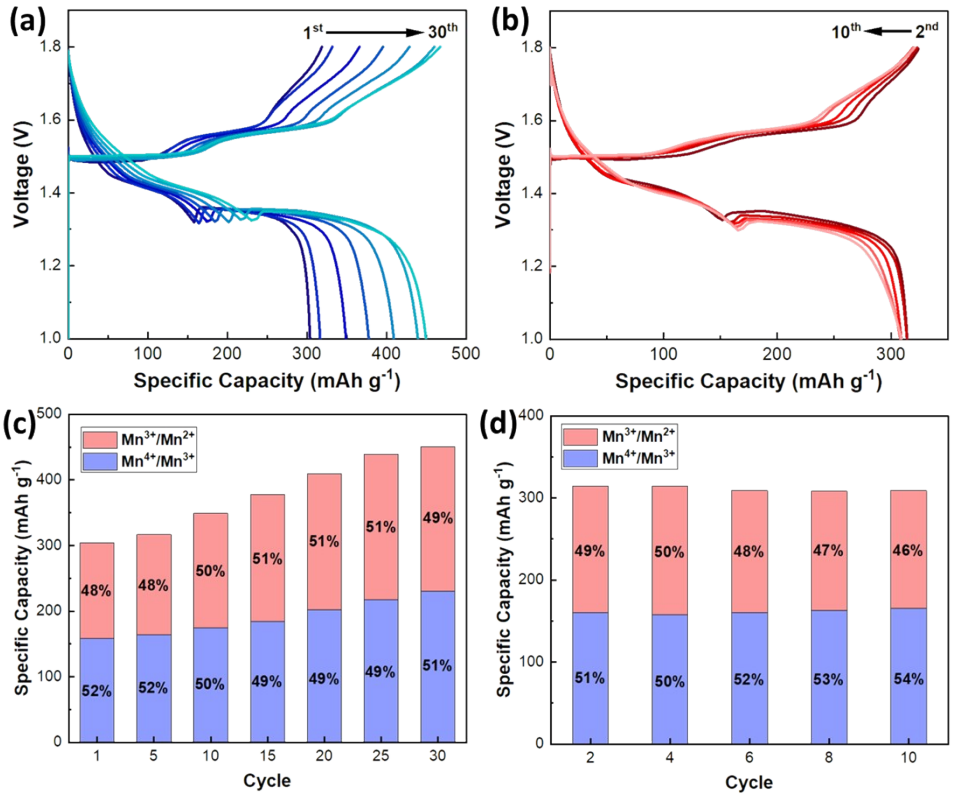

Figure S15. Galvanostatic charge/discharge curves of (a) Zn-doped MnO_2 ZIBs for first 30 cycles and (b) pristine MnO_2 ZIBs for first 10 cycles. Bar chart showing the percentage of capacity contribution of Mn^{4+}/Mn^{3+} and Mn^{3+}/Mn^{2+} redox reactions of (c) Zn-doped MnO_2 ZIBs and (d) pristine MnO_2 ZIBs.

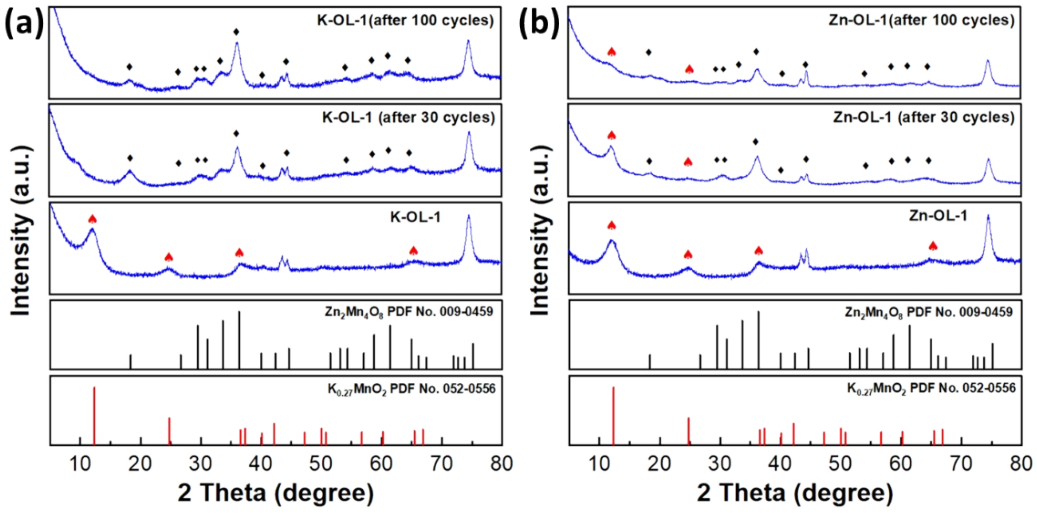

Figure S16. XRD patterns of (a) pristine MnO_2 cathodes and (b) Zn-doped MnO_2 cathodes at the 30th and 100th discharged states.

References

1 H. Tan, J. Verbeeck, A. Abakumov and G. Van Tendeloo, *Ultramicroscopy*, 2012, **116**, 24–33.

2 S. Zhang, K. J. Livi, A. C. Gaillot, A. T. Stone, D. R. Veblen, *American Mineralogist*, 2010, **95(11-12)**, 1741-1746.

3 J. Long, F. Yang, J. Cuan, J. Wu, Z. Yang, H. Jiang, R. Song, W. Song, J. Mao and Z. Guo, *ACS Appl. Mater. Interfaces*, 2020, **12**, 32526–32535.

4 K. W. Nam, S. S. Park, R. dos Reis, V. P. Dravid, H. Kim, C. A. Mirkin and J. F. Stoddart, *Nat. Commun.*, 2019, **10**, 1–10.

5 J. Cao, D. Zhang, Y. Yue, X. Wang, T. Pakornchote, T. Bovornratanaraks, X. Zhang, Z. S. Wu and J. Qin, *Nano Energy*, 2021, **84**, 105876.

6 F. Tang, J. Gao, Q. Ruan, X. Wu, X. Wu, T. Zhang, Z. Liu, Y. Xiang, Z. He and X. Wu, *Electrochim. Acta*, 2020, **353**, 136570.

7 Y. Jiang, D. Ba, Y. Li and J. Liu, *Adv. Sci.*, 2020, DOI:10.1002/advs.201902795.

8 J. Wang, J. G. Wang, H. Liu, Z. You, Z. Li, F. Kang and B. Wei, *Adv. Funct. Mater.*, 2021, DOI:10.1002/adfm.202007397.

9 G. Fang, C. Zhu, M. Chen, J. Zhou, B. Tang, X. Cao, X. Zheng, A. Pan and S. Liang, *Adv. Funct. Mater.*, 2019, **29**, 1–9.

10 S. Khamsanga, R. Pornprasertsuk, T. Yonezawa, A. A. Mohamad and S. Kheawhom, *Sci. Rep.*, 2019, **9**, 1–9.

11 J. Wang, J. G. Wang, X. Qin, Y. Wang, Z. You, H. Liu and M. Shao, *ACS Appl. Mater. Interfaces*, 2020, **12**, 34949–34958.

12 X. Zeng, J. Liu, J. Mao, J. Hao, Z. Wang, S. Zhou, C. D. Ling and Z. Guo, *Adv. Energy Mater.*, 2020, **10**, 1–9.

13 D. Chao, W. Zhou, C. Ye, Q. Zhang, Y. Chen, L. Gu, K. Davey and S. Z. Qiao, *Angew. Chemie - Int. Ed.*, 2019, **58**, 7823–7828.

14 C. Zhong, B. Liu, J. Ding, X. Liu, Y. Zhong, Y. Li, C. Sun, X. Han, Y. Deng, N. Zhao and W. Hu, *Nat. Energy*, 2020, **5**, 440–449.